

Far-Infrared Properties of Lyman Break Galaxies from Cosmological Simulations

Renyue Cen¹

ABSTRACT

Utilizing state-of-the-art, adaptive mesh-refinement cosmological hydrodynamic simulations with ultra-high resolution ($114h^{-1}\text{pc}$) and large sample size (≥ 3300 galaxies of stellar mass $\geq 10^9 M_\odot$), we show how the stellar light of Lyman Break Galaxies at $z = 2$ is distributed between optical/ultra-violet (UV) and far-infrared (FIR) bands. With a single scalar parameter for dust obscuration we can simultaneously reproduce the observed UV luminosity function for the entire range ($3 - 100 M_\odot\text{yr}^{-1}$) and extant FIR luminosity function at the bright end ($\geq 20 M_\odot\text{yr}^{-1}$). We quantify that galaxies more massive or having higher SFR tend to have larger amounts of dust obscuration mostly due to a trend in column density and in a minor part due to a mass (or SFR)-metallicity relation. It is predicted that the FIR luminosity function in the range $\text{SFR} = 1 - 100 M_\odot\text{yr}^{-1}$ is a powerlaw with a slope about -1.7 . We further predict that there is a “galaxy desert” at $\text{SFR}_{\text{FIR}} < 0.02(\text{SFR}_{\text{UV}}/10 M_\odot\text{yr}^{-1})^{2.1} M_\odot\text{yr}^{-1}$ in the $\text{SFR}_{\text{UV}} - \text{SFR}_{\text{FIR}}$ plane. Detailed distributions of SFR_{FIR} at a fixed SFR_{UV} are presented. Upcoming observations by ALMA should test this model. If confirmed, it validates the predictions of the standard cold dark matter model and has important implications on the intrinsic SFR function of galaxies at high redshift.

Subject headings: Methods: numerical, Galaxies: formation, Galaxies: evolution, Galaxies: interactions, intergalactic medium

1. Introduction

The precise relation between optical/UV light detected and dust emission in the far infrared (FIR) of Lyman Break Galaxies (LBGs; Steidel et al. 2003) is difficult to establish observationally, because of the faintness of the expected FIR luminosity (e.g., Ouchi et al. 1999; Adelberger & Steidel 2000). In this work we study this relation using direct simulations of galaxy formation in the standard cosmological constant-dominated cold dark matter model (LCDM; Komatsu et al. 2010) in light of the capabilities of the upcoming Atacama Large

¹Princeton University Observatory, Princeton, NJ 08544; cen@astro.princeton.edu

Millimeter Array (ALMA) mission. The outline of this paper is as follows. In §2 we detail our simulations, method of making galaxy catalogs and a dust obscuration analysis method. Results are presented in §3, followed by conclusions given in §4.

2. Simulations

2.1. Hydrocode and Simulation Parameters

We perform cosmological simulations with the adaptive mesh refinement (AMR) Eulerian hydro code, Enzo (Bryan & Norman 1999; Joung et al. 2009). First we ran a low resolution simulation with a periodic box of $120 h^{-1}\text{Mpc}$ on a side. We identified a region centered on a cluster of mass of $\sim 2 \times 10^{14} M_{\odot}$ at $z = 0$ and then resimulate it with high resolution, embedded in the outer $120 h^{-1}\text{Mpc}$ box. The refined region for “C” run has a size of $21 \times 24 \times 20 h^{-3}\text{Mpc}^3$ and represents 1.8σ fluctuation on that volume. The dark matter particle mass in the refined region is $1.3 \times 10^7 h^{-1} M_{\odot}$. The refined region is surrounded by three layers (each of $\sim 1 h^{-1}\text{Mpc}$) of buffer zones with particle masses successively larger by a factor of 8 for each layer, which then connects with the outer root grid that has a dark matter particle mass 8^4 times that in the refined region. We choose the mesh refinement criterion such that the resolution is always better than $114 h^{-1}\text{pc}$ physical, corresponding to a maximum mesh refinement level of 13 at $z = 0$. The simulations include a metagalactic UV background (Haardt & Madau 1996), a model for shielding of UV radiation by neutral hydrogen (Cen et al. 2005), metallicity-dependent radiative cooling (Cen et al. 1995) extended down to 10 K (Dalgarno & McCray 1972) and all relevant gas chemistry chains for molecular hydrogen formation (Abel et al. 1997), including molecular formation on dust grains (Joung et al. 2009). Star particles are created in cells that satisfy a set of criteria for star formation proposed by Cen & Ostriker (1992). Supernova feedback from star formation is modeled following Cen et al. (2005). We allow the entire feedback processes to be hydrodynamically coupled to surroundings and subject to relevant physical processes, such as cooling and heating. See Cen (2010) for all other simulation details and physical treatments. We use the following cosmological parameters that are consistent with the WMAP7-normalized (Komatsu et al. 2010) LCDM model: $\Omega_M = 0.28$, $\Omega_b = 0.046$, $\Omega_{\Lambda} = 0.72$, $\sigma_8 = 0.82$, $H_0 = 100 h \text{kms}^{-1} \text{Mpc}^{-1} = 70 \text{kms}^{-1} \text{Mpc}^{-1}$ and $n = 0.96$.

2.2. Simulated Galaxy Catalogs

We identify galaxies in our high resolution simulations using the HOP algorithm (Eisenstein & Hu 1999), operated on the stellar particles, which is tested to be robust. Satellites within a galaxy are clearly identified separately. The luminosity of each stellar particle at each of the Sloan

Digital Sky Survey (SDSS) five bands is computed using the GISSEL stellar synthesis code (Bruzual & Charlot 2003), by supplying the formation time, metallicity and stellar mass. Collecting luminosity and other quantities of member stellar particles, gas cells and dark matter particles yields the following physical parameters for each galaxy: position, velocity, total mass, stellar mass, gas mass, mean formation time, mean stellar metallicity, mean gas metallicity, star formation rate, luminosities in five SDSS bands (and various colors) and others. At a spatial resolution of 109pc with nearly 5000 well resolved galaxies at $z = 2$, this simulated galaxy catalog presents an excellent tool to study galaxy formation and evolution.

2.3. Modeling Dust Obscuration

A fully self-consistent modeling would be difficult, given our lack of knowledge of the distribution of dust and its properties. Here we take a simplified approach. Given the 3-d distribution of gas with varying metallicity and stellar particles distributed within it, the observed SFR at a rest-frame UV wavelength λ for the galaxy is computed as

$$\text{SFR}_{\text{UV},\lambda} = \sum_i \text{sfr}_i (1 - e^{-\tau_\lambda(\vec{r}_i \rightarrow \text{obs})}), \quad (1)$$

where $\tau_\lambda(\vec{r} \rightarrow \text{obs})$ is the extinction optical depth at some UV wavelength λ for an individual stellar particle i of star formation rate sfr_i in the galaxy from its individual location \vec{r}_i to the observer:

$$\tau_\lambda(\vec{r} \rightarrow \text{obs}) = (A'_V/1.086) f \beta_\lambda \bar{Z}_i(\vec{r} \rightarrow \text{obs}) N_{H,i}(\vec{r} \rightarrow \text{obs}), \quad (2)$$

where $A'_V = 5.3 \times 10^{-22}$ is visual extinction A_V per unit hydrogen column density per unit solar metallicity for $R_V = 3.1$ (Draine 2011) and $\beta_\lambda \equiv A_\lambda/A_V$ (a fitting function) is taken from Cardelli et al. (1989); $\bar{Z}_i(\vec{r} \rightarrow \text{obs})$ is the column density-weighted mean metallicity of gas obscuring the stellar particle i in solar units and $N_{H,i}(\vec{r} \rightarrow \text{obs})$ is the integrated hydrogen column density from the stellar particle i to the observer. Note that in Equation (1) the calculation is based on 3-d distributions of stellar particles that each are subject to their own integrated optical depth and the sum is over all the member stellar particles, typically of number $10^5 - 10^6$ for a galaxy of stellar mass $10^{11} M_\odot$. In Equation (2) f is a dimensionless parameter that we will adjust such that the simulated LBG UV luminosity function matches observations; f should be of order unity, if dust properties for galaxies at $z \sim 2$ are not drastically different from those derived locally and our galaxy formation model is realistic. As we will see below, the required value of f is indeed close to unity with an adopted extinction law that is also close to those derived locally. Thus, the dust extinction of SFR at a specific UV band is a good proxy of the overall extinction of SFR in the optical-to-UV regime. We will use the 1700Å band for subsequent analysis. The portion of the SFR that

does not escape in UV/optical is assumed to be converted to FIR SFR:

$$\text{SFR}_{\text{FIR}} = \sum_i \text{sfr}_i - \text{SFR}_{\text{UV},\lambda}. \quad (3)$$

For each galaxy we place 95 random observers in its sky at infinity for results presented in the next section. This sampling is adequate and results are converged statistically.

3. Results

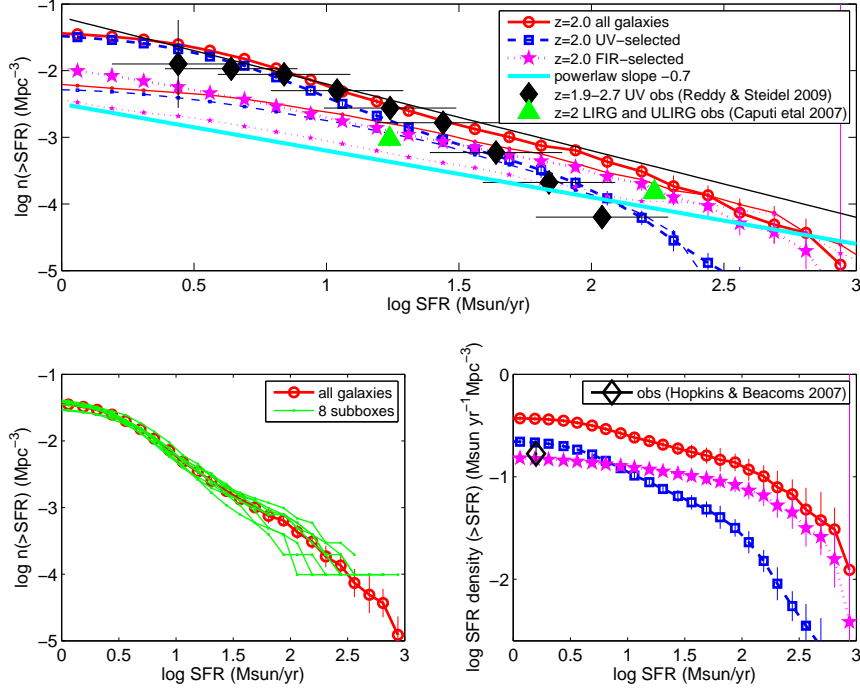


Fig. 1.— *Top panel*: cumulative total SFR function at $z = 2$ (red circles), cumulative UV and FIR SFR functions in blue squares and magenta stars, respectively. Black diamonds are LBG observations $z = 1.9 - 2.7$ from Reddy & Steidel (2009); two green triangles are LIRG and ULIRG observational data from Caputi et al. (2007). We convert to SFR of observational data from $M_{\text{AB}}(1700\text{\AA})$ using the standard conversion formula, $\text{SFR} = 6.1 \times 10^{-[8+0.4M_{\text{AB}}(1700\text{\AA})]} \text{M}_{\odot}/\text{yr}$ (Kennicutt 1998) in the AB magnitude system (Oke 1974). Solid magenta line indicates a powerlaw slope of -0.7 (corresponding to a slope of -1.7 for the differential SFR_{FIR} function). Thin solid black line indicates a powerlaw slope of -1 (corresponding to a slope of -2 for the differential function). The three thin curves of color red, blue and magenta, respectively, correspond their thick counterparts but from a lower resolution simulation with four times poorer spatial and eight times poorer mass resolutions. *Bottom left panel*: the eight green curves represent the cumulative total SFR function in the eight octant volumes; the average of the green curves is the redshift circles (also shown in the top panel). *Bottom right panel*: Cumulative light densities for total (red circles), UV galaxies (blue squares) and FIR galaxies (magenta stars), respectively, at $z = 2$. Also show as a black diamond is the observed data at $z = 2$ compiled by Hopkins & Beacom (2006) with 1σ errorbar.

The top panel of Figure 1 shows the SFR functions for total SFR, UV and FIR selected galaxies, respectively. We have adjusted the parameter f in Equation 2 to be $f = 1.4$ to

arrive at the excellent match between the computed UV SFR function and the observations at $z \sim 2$. We note that f could be 1 if one had adopted a slightly different R_v (Cardelli et al. 1989). In any case, the results with $f = 1$ with $R_v = 3.1$ differ only slightly from the case with $f = 1.4$ shown here and UV SFR function in that case is consistent with the observations within the errorbars. This also suggests that our overall results are robust and insensitive to small variations of uncertain parameters for the dust model within a reasonable range. It also implies that dust properties at $z \sim 2$ are not significantly different from those of local dust.

After matching the observed UV SFR function, we see that the predicted FIR SFR function agrees remarkably well with the observed LIRG and ULIRG data at $z = 2$ (top panel). As a consistency check, we show in the bottom right panel of Figure 1 the cumulative SFR density at $z = 2$. Here we see both the UV SFR density and FIR SFR density agree well with observations. We see that, while the directly observed UV SFR density should be roughly equal to the directly observed FIR SFR density, at face value, the UV SFR density is somewhat higher than FIR SFR density. Our results suggest that galaxies with higher SFR tend to have relatively larger obscuration in UV/optical than galaxies with lower SFR, resulting in a steepening UV luminosity function at the luminous end. The underlying cause will be discussed in Figure 4.

Our previous studies (Cen 2010, 2011) indicate that the “C” run used is positively biased over the cosmic mean by a factor of ~ 2 . Taking that into account, we find that the simulated SFR function as well SFR density becomes too low compared to observed ones. A plausible adjustment is to the stellar IMF. The results shown above uses an top-heavy IMF that produces twice the UV light output per unit SFR than the standard Salpeter function. This provides intriguing evidence for top-heavy IMF at high redshift, consistent with other independent considerations (e.g., Baugh et al. 2005; Davé 2008; van Dokkum 2008). The abundance of massive, rare objects is expected to depend on box size as well as the overdensity of the environment. We assess this effect as follows. We divide the simulation box into eight equal-volume octants and compute the SFR function for each of the eight octants. The results for the eight SFR functions are shown as green curves in the bottom left panel of Figure 1. We note two points here. First, at $\text{SFR} \leq 30 \text{ M}_\odot/\text{yr}$ the SFR function is very well converged and does not appear to sensitively depend on environment. Second, substantial variations are visible at $\text{SFR} \geq 100 \text{ M}_\odot/\text{yr}$, which suggests that the abundance of galaxies with SFR higher than $100 \text{ M}_\odot/\text{yr}$ depends sensitively on density environment and our positively biased simulation box likely has produced some over-abundance of galaxies with $\text{SFR} \geq 100 \text{ M}_\odot/\text{yr}$ relative to galaxies with $\text{SFR} \leq 100 \text{ M}_\odot/\text{yr}$; the computed UV SFR at $\text{SFR} \geq 100 \text{ M}_\odot/\text{yr}$ in this simulation lies above the observed points is thus not inconsistent.

A comparison between the thin and thick curves in the top panel of Figure 1 indicates that the resolutions achieved in the higher resolution run is required in order to provide an

adequate match to observations. The lower (four times spatially and eight times in mass) resolution simulation of the same volume suffers from the two shortcomings. First, there is a slight overproduction of the highest SFR ($\geq 200 \text{ M}_\odot \text{ yr}^{-1}$) galaxies in the lower resolution simulation, which is due to a combination of slight overmerging and higher gas reservoir in the lower resolution run. Second, there is a significant underproduction of lower SFR ($\leq 200 \text{ M}_\odot \text{ yr}^{-1}$) galaxies in the lower resolution simulation due to lower resolution. Taking into account these two effects, the results can be understood and our main predictions on the faint slope and galaxy desert (see below) remain robust.

Our model makes several predictions. The first is that the differential FIR SFR function displays a nearly perfect powerlaw of slope about -1.7 below $\text{SFR}_{\text{FIR}} \sim 100 \text{ M}_\odot/\text{yr}$ at $z = 2$. We attribute this outcome to a combination of three physical factors: (1) the intrinsic differential SFR function is steeper than -1.7 but close to -2 , as indicated by the thin black line in the top panel of Figure 1; (2) on average, higher SFR galaxies have higher dust optical depth (as discussed in detail in Figure 4 below) that tends to flatten the FIR SFR function; (3) there is a significant dispersion of SFR_{FIR} at a fixed intrinsic SFR (see Figure 2 below) that also smoothes and flattens the FIR SFR function. This predictions can be tested by ALMA observations, and if confirmed, will provide evidence that the intrinsic SFR function is close to a powerlaw with a slope that is steeper than -1.7 in the SFR range $10 - 300 \text{ M}_\odot \text{ yr}^{-1}$. We attribute this behavior to a large dispersion of SFR at a fixed halo mass but will address it in more detail separately.

Given this slope, most of the FIR light is concentrated at the bright end. In terms of cumulative galaxy number density we find that UV and FIR selected samples are expected to have comparable abundances at $\text{SFR} \geq 20 - 40 \text{ M}_\odot/\text{yr}$. In terms of cumulative SFR density we find that FIR selected galaxies with $\text{SFR} \geq 10 \text{ M}_\odot/\text{yr}$ dominate over UV selected galaxies with $\text{SFR} \geq 10 \text{ M}_\odot/\text{yr}$; the reverse is true at $\text{SFR} < 10 \text{ M}_\odot/\text{yr}$. Reading directly from simulations we find that FIR selected galaxies with $\text{FIR SFR} \geq 10 \text{ M}_\odot/\text{yr}$ contain 78% of total FIR light density, whereas UV selected galaxies with $\text{UV SFR} \geq 10 \text{ M}_\odot/\text{yr}$ contain only 50% (the actual number may be still lower, since our simulations likely have underestimated the number density of galaxies below $\text{SFR} \leq 3 \text{ M}_\odot/\text{yr}$, below which a flattening of the UV SFR function is seen in the top panel of Figure 1). Note that while a Schechter function normally fits halo functions well, it does not provide an adequate fit to the FIR SFR function, due to large dispersions of SFR at fixed halo masses mentioned above. Our results suggest that the observed UV-selected LBGs detected at $\text{SFR} \geq \text{a few } \text{M}_\odot/\text{yr}$ at $z = 2 - 3$ can account for the bulk of the FIR background at $z \sim 2 - 3$, consistent with earlier independent observational assessments (e.g., Smail et al. 1999; Adelberger & Steidel 2000; Chapman & Casey 2009).

Needless to say, our model implies that UV and FIR selected galaxies form a complementary pair of populations that are drawn from the same underlying general galaxy

population. This point has been noted by others (e.g., Sawicki & Yee 1998; Meurer et al. 1999; Shapley et al. 2001; Papovich et al. 2001; Calzetti 2001).

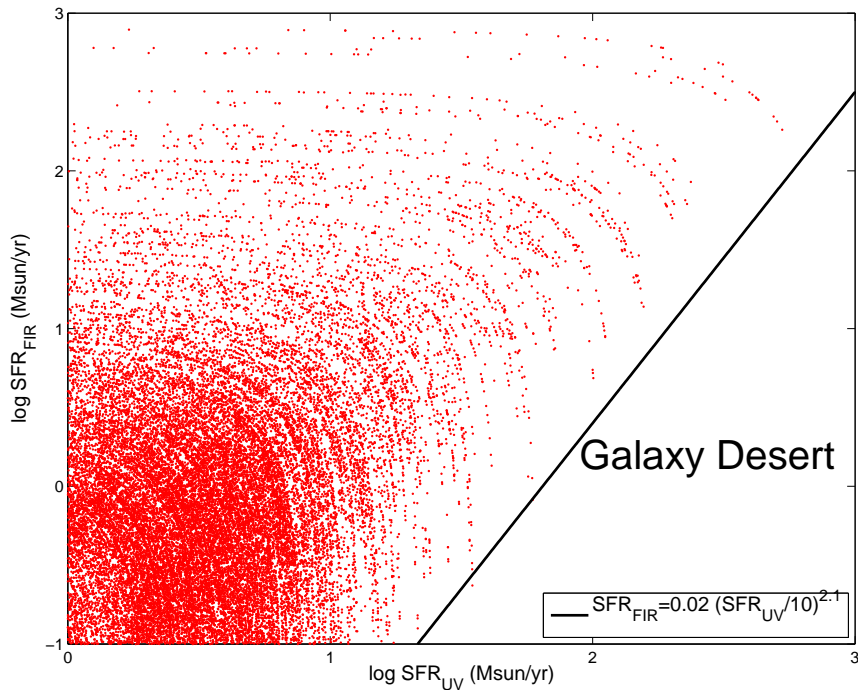


Fig. 2.— each dot is a galaxy in the plane of UV and FIR detected SFR at $z = 2$. The solid line is $\text{SFR}_{\text{FIR}} = 0.02[\text{SFR}_{\text{UV}}/10 \text{ M}_{\odot}\text{yr}^{-1}]^{2.1} \text{ M}_{\odot}\text{yr}^{-1}$.

Figure 2 shows a scatter plot of galaxies in the $\text{SFR}_{\text{UV}} - \text{SFR}_{\text{FIR}}$ plane. We see a nearly complete empty space at the lower right corner of the plot, with $\text{SFR}_{\text{FIR}} < 0.02[\text{SFR}_{\text{UV}}/10 \text{ M}_{\odot}\text{yr}^{-1}]^{2.1} \text{ M}_{\odot}\text{yr}^{-1}$, which we shall call the “galaxy desert”. The physical reason for this nearly complete absence of galaxies with high UV SFR and low FIR SFR rate is that the dust optical depth of galaxies increases with SFR. This second prediction of our model should be testable by ALMA observations.

Figure 3 dissects the information contained in Figure 2 further and shows a set of

Table 1. Parameters for gaussians in Figure 3 with $\log \text{SFR}_{\text{UV}}$ being the variable

| $\text{SFR}_{\text{UV}} (\text{M}_{\odot}/\text{yr})$ | mean | dispersion |
|---|-------|------------|
| 3-10 | -0.84 | 1.0 |
| 10-30 | 0.030 | 0.98 |
| 30-100 | 0.85 | 0.76 |
| 100-300 | 1.7 | 0.72 |

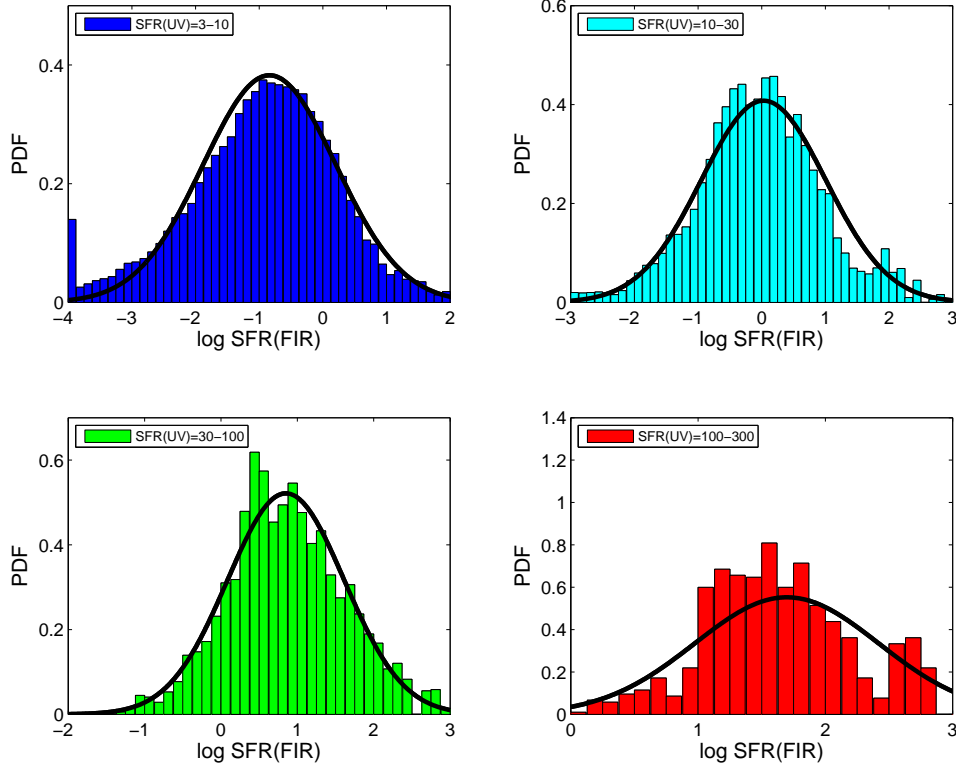


Fig. 3.— shows four distributions of FIR SFR for LBG galaxies at each of the four UV SFR values of $3 - 10 M_{\odot}/\text{yr}$ (top left), $10 - 30 M_{\odot}/\text{yr}$ (top right), $30 - 100 M_{\odot}/\text{yr}$ (bottom left) and $100 - 300 M_{\odot}/\text{yr}$ (bottom right), respectively, at $z = 2$. Each black curve is a gaussian fit with its parameters listed in Table 1.

distributions of SFR_{FIR} at a given range of SFR_{UV} . We see that for LBGs with $\text{SFR}_{\text{UV}} = 10 - 100 M_{\odot}/\text{yr}$, the distributions are well fitted by gaussians (the black curves) using $\log \text{SFR}_{\text{UV}}$ as the variable. In the lowest SFR_{UV} ($\text{SFR}_{\text{UV}} = 3 - 10 M_{\odot}/\text{yr}$) we see a slight tendency of the SFR_{FIR} distribution to skew towards the low SFR_{FIR} end, indicative of increasingly diminishing dust obscuration for galaxies with low SFR. In the highest SFR_{UV} ($\text{SFR}_{\text{UV}} = 100 - 300 M_{\odot}/\text{yr}$), the SFR_{FIR} distribution is significantly skewed to the high SFR_{FIR} end for the same physical reason. We list the parameters of the best gaussian fit of SFR_{FIR} distributions for all SFR_{UV} bins in Table 1. These predictions should be verifiable by ALMA observations.

Finally, we examine the underlying cause of the generally differential rate of dust obscuration seen in prior figures where higher SFR galaxies are more dust obscured. Figure 4 shows gas metallicity and gas column density as a function of stellar mass and total SFR, respectively. Examination of the top left panel of Figure 4 indicates that in the stellar mass range $M_{\text{star}} \geq 10^{10} M_{\odot}$ there is a positive correlation between gas metallicity and stellar mass, in agreement with the observed, so-called mass-metallicity relation at $z \sim 2$ of Erb et al. (2006). While this is not the focus of our study here, the agreement is quite

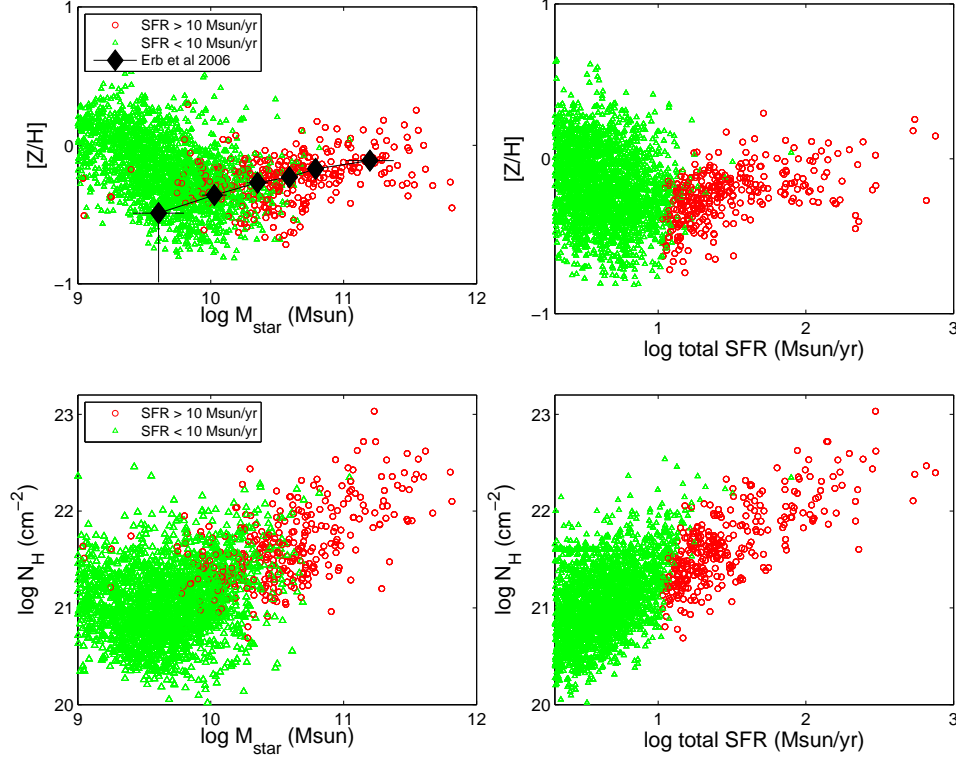


Fig. 4.— *Top left panel:* column density weighted gas metallicity averaged over the entire galaxy as a function of stellar mass. Shown in black diamond is observations from Erb et al. (2006) at $z \sim 2$. *Top right panel:* column density weighted gas metallicity averaged over the entire galaxy as a function of SFR. *Bottom left panel:* radially integrated total column density as a function of stellar mass. *Bottom right panel:* radially integrated total column density as a function of SFR. In all the panels red symbols have SFR greater than $10 \text{ M}_{\odot}/\text{yr}$ and green symbols less than $10 \text{ M}_{\odot}/\text{yr}$.

remarkable but consistent with the agreement that is found between simulations and observations with respect to the metallicity distribution of damped Lyman alpha systems in an earlier study (Cen 2010). A comparison between the two top and two bottom panels of Figure 4 clearly indicates that the correlation between column density and stellar mass or SFR is about three times stronger than that between gas metallicity and stellar mass or SFR. This suggests that the general trend of larger dust obscuration for larger stellar mass or SFR is mostly due to a trend in column density in the same sense, but positively aided by a mass (or SFR)-metallicity trend. This overall trend gives an integral constraint on the total optical depth. The actual distribution of dust optical depth at a given galaxy mass (or SFR) or even for a given galaxy viewed at different angles has large dispersions due to the clumpy distribution of gas with varying metallicity, resulting in a wide FIR SFR distribution within a narrow UV SFR range, as quantified in Figure 3.

4. Conclusions

Using state-of-the-art, adaptive mesh-refinement Eulerian cosmological hydrodynamic simulations with high resolution ($114h^{-1}\text{pc}$), large sample size (≥ 3300 galaxies of stellar mass $\geq 10^9 M_\odot$) and a physically sound treatment of relevant processes, we examine the properties of LBGs at $z = 2$ with respect to their partitioning of UV and FIR light. Using a single scalar parameter that relates the amount of dust obscuration to the product of hydrogen column density and gas metallicity to model dust obscuration along each line of sight (i.e., a dust extinction law derived in our local universe), we find that the observed UV luminosity function for the entire range and FIR luminosity function at the bright end can be simultaneously reproduced. Our theoretical modeling affirms the aesthetically appealing picture where UV and FIR selected galaxies at $z \sim 2$ are drawn from the same general galaxy population. The observationally different manifestations are merely due to the known fact that each galaxy is seen through its own unique set of dust screens at a given viewing angle. Star forming galaxies that are more massive or have higher SFR tend to have larger amounts of dust obscuration at high redshift.

We predict that the FIR luminosity function in the range $\text{SFR} = 1 - 100 M_\odot/\text{yr}$ is a powerlaw with a slope -1.7 with uncertainty of ~ 0.1 . We further predict that there is a “galaxy desert” at $\text{SFR}_{\text{FIR}} < 0.02(\text{SFR}_{\text{UV}}/10 M_\odot\text{yr}^{-1})^{2.1} M_\odot\text{yr}^{-1}$ in the $\text{SFR}_{\text{UV}} - \text{SFR}_{\text{FIR}}$ plane. Detailed distributions of SFR_{FIR} at an observed SFR_{UV} are quantified and can be used to further test the model. We expect that upcoming observations by ALMA should be able to test these predictions hence ultimately the standard cosmological model with respect to its properties on sub-megaparsec scales. If ALMA observations confirms the predicted faint end slope of the FIR luminosity function, it would imply that the intrinsic SFR function of galaxies may be closer to a powerlaw of a slope at least as steep as -2 in the range $\text{SFR} = 3 - 100 M_\odot$ than a Schechter function.

I would like to thank Computing resources were in part provided by the NASA High- End Computing (HEC) Program through the NASA Advanced Supercomputing (NAS) Division at Ames Research Center. I thank an anonymous referee for a constructive report. This work is supported in part by grants NAS8-03060 and NNX11AI23G.

REFERENCES

- Abel, T., Anninos, P., Zhang, Y., & Norman, M. L. 1997, *New Astronomy*, 2, 181
- Adelberger, K. L., & Steidel, C. C. 2000, *ApJ*, 544, 218

- Baugh, C. M., Lacey, C. G., Frenk, C. S., Granato, G. L., Silva, L., Bressan, A., Benson, A. J., & Cole, S. 2005, *MNRAS*, 356, 1191
- Bruzual, G., & Charlot, S. 2003, *MNRAS*, 344, 1000
- Bryan, G. L., & Norman, M. L. 1999, in *Structured Adaptive Mesh Refinement Grid Methods*, ed. N. P. C. S. B. Baden (IMA Volumes on Structured Adaptive Mesh Refinement Methods, No. 117), 165
- Calzetti, D. 2001, *PASP*, 113, 1449
- Caputi, K. I., Lagache, G., Yan, L., Dole, H., Bavouzet, N., Le Floch, E., Choi, P. I., Helou, G., & Reddy, N. 2007, *ApJ*, 660, 97
- Cardelli, J. A., Clayton, G. C., & Mathis, J. S. 1989, *ApJ*, 345, 245
- Cen, R. 2010, *ArXiv e-prints*
- . 2011, *ApJ*, in press, arXiv1104.5046
- Cen, R., Kang, H., Ostriker, J. P., & Ryu, D. 1995, *ApJ*, 451, 436
- Cen, R., Nagamine, K., & Ostriker, J. P. 2005, *ApJ*, 635, 86
- Cen, R., & Ostriker, J. P. 1992, *ApJ*, 399, L113
- Chapman, S. C., & Casey, C. M. 2009, *MNRAS*, 398, 1615
- Dalgarno, A., & McCray, R. A. 1972, *ARA&A*, 10, 375
- Davé, R. 2008, *MNRAS*, 385, 147
- Draine, B. T. 2011, *Physics of the Interstellar and Intergalactic Medium*, ed. Draine, B. T.
- Eisenstein, D., & Hu, P. 1999, *ApJ*, 511, 5
- Erb, D. K., Shapley, A. E., Pettini, M., Steidel, C. C., Reddy, N. A., & Adelberger, K. L. 2006, *ApJ*, 644, 813
- Haardt, F., & Madau, P. 1996, *ApJ*, 461, 20
- Heckman, T. M. 2001, in *Astronomical Society of the Pacific Conference Series*, Vol. 240, *Gas and Galaxy Evolution*, ed. J. E. Hibbard, M. Rupen, & J. H. van Gorkom, 345
- Hopkins, A. M., & Beacom, J. F. 2006, *ApJ*, 651, 142
- Joung, M. R., Cen, R., & Bryan, G. L. 2009, *ApJ*, 692, L1

- Kennicutt, Jr., R. C. 1998, *ARA&A*, 36, 189
- Komatsu, E., Smith, K. M., Dunkley, J., Bennett, C. L., Gold, B., Hinshaw, G., Jarosik, N., Larson, D., Nolte, M. R., Page, L., Spergel, D. N., Halpern, M., Hill, R. S., Kogut, A., Limon, M., Meyer, S. S., Odegard, N., Tucker, G. S., Weiland, J. L., Wollack, E., & Wright, E. L. 2010, ArXiv e-prints
- Meurer, G. R., Heckman, T. M., & Calzetti, D. 1999, *ApJ*, 521, 64
- Oke, J. B. 1974, *ApJS*, 27, 21
- Ouchi, M., Yamada, T., Kawai, H., & Ohta, K. 1999, *ApJ*, 517, L19
- Papovich, C., Dickinson, M., & Ferguson, H. C. 2001, *ApJ*, 559, 620
- Reddy, N. A., & Steidel, C. C. 2009, *ApJ*, 692, 778
- Sawicki, M., & Yee, H. K. C. 1998, *AJ*, 115, 1329
- Shapley, A. E., Steidel, C. C., Adelberger, K. L., Dickinson, M., Giavalisco, M., & Pettini, M. 2001, *ApJ*, 562, 95
- Smail, I., Ivison, R. J., Kneib, J.-P., Cowie, L. L., Blain, A. W., Barger, A. J., Owen, F. N., & Morrison, G. 1999, *MNRAS*, 308, 1061
- Steidel, C. C., Adelberger, K. L., Adelberger, K. L., Shapley, A. E., Pettini, M., Dickinson, M., & Giavalisco, M. 2003, *ApJ*, 592, 728
- van Dokkum, P. G. 2008, *ApJ*, 674, 29